Journal of Biomedical Optics

BiomedicalOptics.SPIEDigitalLibrary.org

Development of a blood oxygenation phantom for photoacoustic tomography combined with online pO_2 detection and flow spectrometry

Marcel Gehrung
Sarah E. Bohndiek
Joanna Brunker

SPIE.

Marcel Gehrung, Sarah E. Bohndiek, Joanna Brunker, "Development of a blood oxygenation phantom for photoacoustic tomography combined with online pO_2 detection and flow spectrometry," *J. Biomed. Opt.* **24**(12), 121908 (2019), doi: 10.1117/1.JBO.24.12.121908.

Journal of Biomedical Optics 24(12), 121908 (December 2019)

Development of a blood oxygenation phantom for photoacoustic tomography combined with online pO_2 detection and flow spectrometry

Marcel Gehrung,[a,b] Sarah E. Bohndiek,[a,b] and Joanna Brunker[a,b,*]
[a]Cancer Research UK Cambridge Institute, Li Ka-Shing Centre, Cambridge, United Kingdom
[b]University of Cambridge, Department of Physics, Cambridge, United Kingdom

Abstract. Photoacoustic tomography (PAT) is intrinsically sensitive to blood oxygen saturation (sO_2) *in vivo*. However, making accurate sO_2 measurements without knowledge of tissue- and instrumentation-related correction factors is extremely challenging. We have developed a low-cost flow phantom to facilitate validation of PAT systems. The phantom is composed of a flow circuit of tubing partially embedded within a tissue-mimicking material, with independent sensors providing online monitoring of the optical absorption spectrum and partial pressure of oxygen in the tube. We first test the flow phantom using two small molecule dyes that are frequently used for photoacoustic imaging: methylene blue and indocyanine green. We then demonstrate the potential of the phantom for evaluating sO_2 using chemical oxygenation and deoxygenation of blood in the circuit. Using this dynamic assessment of the photoacoustic sO_2 measurement in phantoms in relation to a ground truth, we explore the influence of multispectral processing and spectral coloring on accurate assessment of sO_2. Future studies could exploit this low-cost dynamic flow phantom to validate fluence correction algorithms and explore additional blood parameters such as pH and also absorptive and other properties of different fluids. [DOI: 10.1117/1.JBO.24.12.121908]

Keywords: blood oxygenation; flow; phantom; photoacoustic tomography.

Paper 190183SSRR received Jun. 3, 2019; accepted for publication Sep. 9, 2019; published online Oct. 17, 2019.

1 Introduction

Photoacoustic tomography (PAT) exploits optically generated ultrasound to provide images that combine the high contrast and spectral specificity of optical imaging with the high spatial resolution of ultrasound. In particular, PAT has been widely used to image blood hemoglobin concentration and oxygenation, which have the potential to inform on a range of pathophysiologies, from tumor aggressiveness[1] and treatment response[2,3] to intestinal inflammation associated with Crohn's disease[4] and colitis.[5] The derivation of such images is usually based on spectral unmixing to resolve the differential absorption contributions of oxy- (HbO_2) and deoxyhemoglobin (Hb). Total hemoglobin concentration (THb) is typically taken as the sum of the contributions to the photoacoustic signal $P(\mathbf{r},\lambda)$ from HbO_2 and Hb, whereas hemoglobin oxygenation (sO_2) is taken as the ratio of HbO_2 to THb.

Unfortunately, the assessment of HbO_2 and Hb content from photoacoustic data is not trivial. Estimation of these chromophore concentrations from images taken at multiple wavelengths is commonly achieved using least-squares fitting of reference HbO_2 and Hb spectra,[6] which are tabulated in the literature;[7–9] however, these absorption spectra are recorded under *in vitro* conditions thus can vary substantially from the attenuation spectra (incorporating both absorption and scattering) experienced within an *in vivo* study. Moreover, the measured photoacoustic signal $P(\mathbf{r},\lambda)$ is not directly proportional to the absorbed energy density $H(\mathbf{r},\lambda)$. $H(\mathbf{r},\lambda)$ is the product of the light fluence Φ, which itself varies as a function of $\mathbf{r}$ and λ, as well as $\mu_a(\mathbf{r},\lambda)$ and the reduced scattering coefficient $\mu_s'(\mathbf{r},\lambda)$

$$H(\mathbf{r},\lambda) = \mu_a(\mathbf{r},\lambda)\Phi[\mathbf{r},\lambda,\mu_a(\mathbf{r},\lambda),\mu_s'(\mathbf{r},\lambda)]. \quad (1)$$

This codependence of $H(\mathbf{r},\lambda)$ on both absorption and light fluence leads to an effect known as "spectral coloring," where variations in local fluence bias the measured optical absorption distribution.[10,11] Alternative approaches beyond the standard linear unmixing model have been shown to improve sO_2 measurement accuracy, in particular by accounting for the light fluence distribution through: internal irradiation,[12] diffusion theory modeling,[13–17] Monte Carlo simulations,[18] model-based iterative minimisation,[19–21] and linear superposition of reference fluence base spectra.[22]

Several studies have explored ways to validate photoacoustic images using phantoms with well-characterized optical and acoustic properties.[23,24] Validation of photoacoustically measured sO_2 is possible using CO-oximetry,[13,25,26] pulse oximetry,[27] and blood-gas analysis;[28] correlation between pO_2 and sO_2 has also been used to study oxygen–hemoglobin binding.[29] However, most studies have worked with static blood samples with limited control on the sO_2. Allowing blood to flow in a circuit[13,26] and with the ability to vary the sO_2 provides a more versatile platform for investigating PAT oxygenation measurements.

In this work, we created a low-cost flow circuit with online monitoring to facilitate validation of PAT systems. The phantom was tested by circulating different concentrations of methylene blue (MB) and indocyanine green (ICG). The phantom was then applied to explore the accuracy of sO_2 assessment using PAT,

*Address all correspondence to Joanna Brunker, E-mail: jb2014@cam.ac.uk

with sO_2 values ranging from 0% to 100%. We studied the impact of evaluating sO_2 using different reference spectra for HbO_2 and Hb, and also the effect of spectral coloring, showing discrepancies of up to 60% between the actual and measured sO_2. Our findings highlight the importance of careful choice of spectra for unmixing and the development of fluence correction models to improve the biological relevance of sO_2 measurements derived from PAT images.

2 Methods

2.1 *Flow System*

The flow system (Fig. 1) enables fluids to be circulated within a vessel-mimicking tube embedded in a tissue-mimicking agar phantom placed in the chamber of a photoacoustic imaging system. Online (and offline) spectrometry and pO_2 detection provide independent validation of the spectral measurements made by the imaging system. Details of the tissue-mimicking phantom, the photoacoustic imaging system, the spectrometric validation, the pO_2 detection, and the spectral analysis are described in the following sections.

2.1.1 *Tissue-mimicking phantom*

The tissue-mimicking phantom used for photoacoustic imaging comprised either static or flowing fluids within a tube (vessel) embedded within an agar (tissue) cylinder, 19 mm in diameter. Agar phantoms were prepared by heating a solution of 1.5% w/v agar (05039, Fluka) in water, and then adding 2.1% v/v Intralipid (I141, Sigma-Aldrich), before pouring into an open 20 mL syringe (with the injection end removed), in the center of which was positioned a needle supporting the tubing vertically. The solidified agar phantom had a scattering coefficient of 5 cm^{-1} due to the Intralipid, but the absorption coefficient was assumed to be negligible.

To provide optical absorption for assessment of spectral coloring, nigrosin (198285, Sigma-Aldrich) was also added to the tissue-mimicking phantom formulation to produce phantoms with an absorption coefficient of 0.05 or 0.1 cm^{-1} at 564 nm (the peak of the nigrosin spectrum).

2.1.2 *Photoacoustic tomography*

For photoacoustic imaging, a small animal imaging system [MultiSpectral Optoacoustic Tomography (MSOT) inVision 256-TF, iThera Medical] was used. Briefly, a tunable optical parametric oscillator pumped by an Nd:YAG laser provides excitation pulses with a duration of 9 ns at wavelengths from 660 to 1300 nm at a repetition rate of 10 Hz with a wavelength tuning speed of 10 ms and a peak pulse energy of 90 mJ at 720 nm. Ten arms of a fiber bundle provide near-uniform illumination over a disk extending ~8 mm along the imaging chamber. Photoacoustic signals are detected using 256 toroidally focused ultrasound transducers with a center frequency of 5 MHz (60% bandwidth), organized in a concave array of 270-deg angular coverage, and a radius of curvature of 4 cm.

2.1.3 *Detection of pO_2*

Two oxygen fluorescence quenching needle probes (NX-BF/O/E, Oxford Optronix) were inserted into the flow circuit before and after the tissue-mimicking phantom. A touch-screen monitor (OxyLite Pro, Oxford Optronix) displayed the temperature

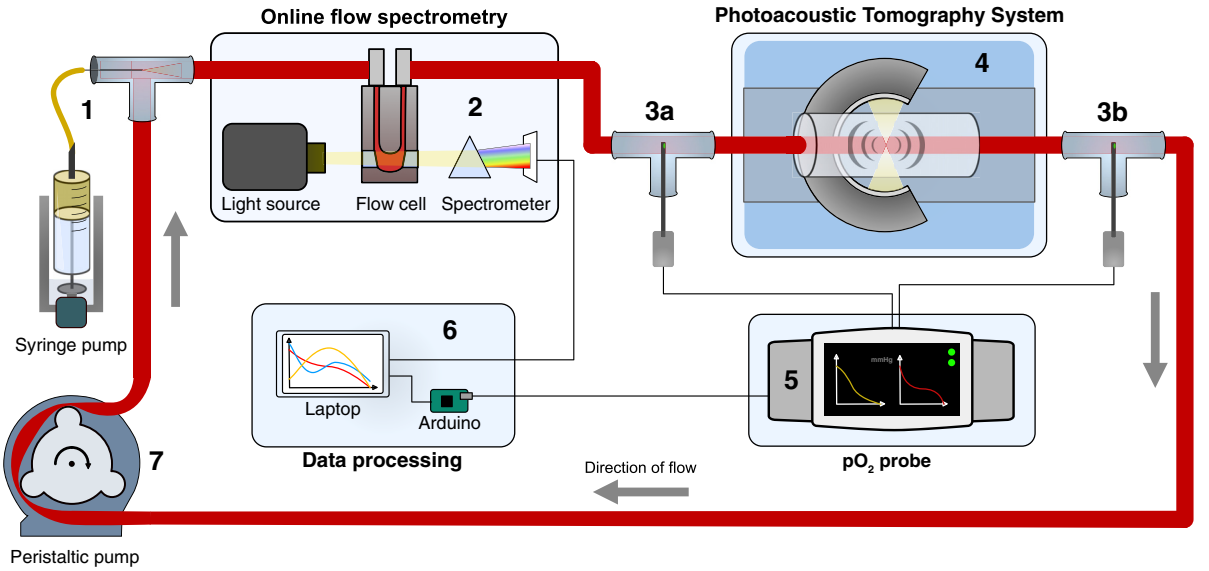

Fig. 1 Overview of the flow system. (1) Injection site for introducing oxygenated blood (or other fluids) into the flow system, and for subsequently deoxygenating the blood using sodium hydrosulfite delivered via the syringe driver (MKCB2159V, Harvard); (2) online spectra are recorded using a light source (Avalight-HAL-S-Mini, Avantes) and spectrometer (AvaSpec-ULS2048-USB2-VA-50, Avantes) as the blood passes through a flow cell (170700-0.5-40, Hellma Analytics); (3) needle probes (NX-BF/O/E, Oxford Optronix) measure the temperature and partial pressure of oxygen (pO_2) before (3a) and after (3b) the blood passes through an agar phantom immersed in the photoacoustic imaging system (MSOT inVision 256-TF, iThera Medical) (4); (5) a touch-screen monitor (OxyLite Pro, Oxford Optronix) displays temperature and oxygen data; (6) these data are downloaded via an Arduino UNO and read in MATLAB on a laptop, which also records the spectrometer readings via AvaSoft software; (7) a peristaltic pump (CTP100, Fisher Scientific) provides blood circulation.

and partial pressure of oxygen (pO_2) real-time, and these data were downloaded via an Arduino UNO and read in MATLAB. The two measurements before and after the phantom were near-identical but were recorded so that the mean value could be used to estimate the pO_2 (and temperature) at the photoacoustic imaging site. The relationship between the oxygen saturation (sO_2) and the partial pressure (pO_2) in blood is described by the characteristic sigmoid-shaped oxygen–hemoglobin dissociation curve. A widely accepted fit to this curve is given by the Severinghaus equation:[30,31]

$$sO_2(\%) = \frac{100}{[23400 \times (pO_2)^3 + 150 \times (pO_2)]^{-1} + 1}, \quad (2)$$

which was used to convert our pO_2 measurements into sO_2.

2.1.4 *Online flow spectrometry*

Absorption spectra were recorded once per second via AvaSoft software using a light source (Avalight-HAL-S-Mini, Avantes) and spectrometer (AvaSpec-ULS2048-USB2-VA-50, Avantes) as the fluid passed through a flow cell (170700-0.5-40, Hellma Analytics).

2.1.5 *Offline spectrometry*

To independently validate spectrophotometric measurements made in the flow circuit, optical absorbance spectra were also recorded offline using a microplate spectrometer (CLARIOstar, BMG LABTECH). Fluid samples were measured in a 48-well plate (Corning Costar).

2.2 *Flow System Characterization*

2.2.1 *Tubing assessment*

The optimum tubing was determined by comparing photoacoustic images obtained of agar phantoms containing various tube types filled with a 25-μmol ICG solution (Sigma-Aldrich I2633). The tubes were labeled according to their nominal inner and outer diameters (I.D/O.D.) in μm but were also made of different materials: polypropene 2660/2800 (Alliance Online PSTS0007); THV500 2800/3150, 500/600 (Paradigm Optics); silicone 1570/2410, 630/1190, 300/630 (VWR 228-0256, 228-0254, 228-0253); PVC 1500/2100 (VWR 228-3857); PMMA 667/1000, 432/865, 375/500 (Paradigm Optics); polythene 580/960 (Smiths Medical 800/100/200 12665497).

2.2.2 *Dye dilution series*

A dilution series was used to demonstrate the utility of the flow circuit for injecting different fluids into the closed PAT system, allowing PAT to be performed concurrently with online spectrometry. MB (50484, Fluka) and ICG (I2633, Sigma-Aldrich) solutions were prepared by diluting concentrations of 500 and 100 μM (for MB and ICG, respectively) in deionized water. First, four spectra were measured and averaged for samples of each concentration placed in a 48-well plate in the CLARIOstar spectrophotometer. The concentrations were then flushed individually through the flow system, starting with deionized water and then sequentially with increasing concentration. Ten online spectra were recorded over a range of 333 to 1100 nm, and 10 single-slice PA images (no pulse-to-pulse averaging) were acquired for 17 wavelengths (660, 664, 680, 684, 694, 700, 708, 715, 730, 735, 760, 770, 775, 779, 800, 850, and 950 nm), taking the mean of the 10 single-slice images for each concentration. The circuit was flushed with water between each concentration.

2.2.3 *Dynamic concentration change*

A dynamic concentration change was used to illustrate the possibility for real-time spectroscopic and photoacoustic measurements. Continuous acquisition of online spectra and single-slice photoacoustic images was commenced once deionized water was circulating within the flow system. After a certain time, a high concentration dye solution (either 500 μM MB or 100 μM ICG) was injected using the syringe pump (at 100 μL/min). It was verified that during the estimated few seconds taken for fluid to pass from the online spectrometer to the photoacoustic imaging slice, the changes in the online spectra were insignificant and therefore the acquired spectra could be used to unmix the synchronized photoacoustic images.

The amount (moles) of the dye $Q(t)$ in the circuit at any given time t can be modeled using a first-order differential equation. In Eq. (3), the rate of change $dQ(t)/dt$ is equal to the difference between the inflow and outflow amounts, expressed in terms of the flow rate F induced by the syringe pump (100 μL/min), the concentration c of dye injected (500 or 100 μM) and the volume V (5 mL) of circulating fluid:

$$\frac{dQ(t)}{dt} = F\left[c - \frac{Q(t)}{V}\right]. \quad (3)$$

The initial condition is given by Eq. (4), giving rise to Eq. (5), which is the solution for the dye concentration Q/V as a function of time. In the limit $t \to \infty$, $Q(t)/V \to c$, as expected:

$$Q(0) = Q_0 = 0; \quad (4)$$

$$\frac{Q(t)}{V} = c\left[1 - e^{-\frac{F}{V}t}\right]. \quad (5)$$

2.3 *Blood Oxygenation Measurements*

Mouse blood, predominantly made up of strains B6 and 129SvEv, was collected post mortem from the animal facility at the Cancer Research UK Cambridge Institute, complying with the UK Animals (Scientific Procedures) Act 1986. Each mouse contributed about 1 mL to a pool of ~5 mL blood required for the flow circuit. Chemicals were added to preserve, oxygenate, and deoxygenate the blood. Prior to the experiment, ethylenediaminetetraacetic acid anticoagulant (9002-07-7, Sigma-Aldrich) was added to the fresh blood, which was kept in a refrigerator under 4°C for no more than 72 hours. During the experiment, the blood was returned to room temperature, and the oxygenation was controlled chemically by adding 0.2% v/v hydrogen peroxide, H_2O_2 (7722-84-1, Sigma-Aldrich), for oxygenation[32] and sodium hydrosulfite (7775-14-6, ACROS Organics) for deoxygenation.[33] The sodium hydrosulfite was dissolved in phosphate-buffered saline (PBS) ~0.03% w/v for injection into the flow circuit.

2.4 *Spectral and Statistical Analysis*

PAT contrast is provided by optical absorbers within the field of illumination and detection. In general, PAT does not have

sufficient resolution to visualize individual molecules and therefore each image pixel (or voxel) corresponds to more than one optical absorber, and a "spectral unmixing" approach is required in order to extract the individual spectral components. The linear mixture model[34] assumes that the measured spectrum is a linear combination of distinct spectra:

$$\mathbf{x} = \mathbf{SC} + n, \tag{6}$$

where $\mathbf{x}$ is the M-wavelength $\times$ N-pixels measurement matrix, $\mathbf{S}$ is the $M \times K$ matrix of K spectra (end-members), $\mathbf{C}$ is the unknown $K \times N$ matrix of end-member abundances (concentrations), and n is measurement noise. Neglecting n, an estimation $\hat{\mathbf{C}}$ of the absorber concentrations can be calculated from Eq. (6) by solving the following least-squares problem:[11,35]

$$\hat{\mathbf{C}} = \arg\min_{C} \|\mathbf{SC} - \mathbf{x}\|_2^2, \tag{7}$$

with the solution

$$\hat{\mathbf{C}} = \mathbf{xS}^{+}, \tag{8}$$

where $\mathbf{S}^{+}$ is the pseudoinverse of $\mathbf{S}$. The performance of spectral unmixing carried out on acquired PA images was compared using three different spectra: those from the literature,[7–9] and those experimentally measured in this study, from either the online spectrometer cell or the offline plate reader. In addition, the online flow spectra were used to provide an independent ground truth for sO_2; this entailed unmixing of the online flow spectra with the spectra for oxy- and deoxyhemoglobin also measured live during the experiments.

To correct for the spectrally varying fluence (spectral coloring) when using optically absorbing phantoms, the image intensities in the tube region were divided by the nigrosin absorption spectrum. Specifically, the nigrosin absorption spectrum was normalized to the known absorption coefficient (at the 564-nm absorption maximum) and resampled at the 17-experimental wavelengths; the multispectral PA data were then divided by a wavelength-specific factor calculated from exponential decay over the 8.5 mm distance from the outer edge of the phantom (the background agar material impregnated with absorbing nigrosin) to the tube wall. All data and source code used in this publication are available at https://doi.org/10.17863/CAM.40365 and in a GitHub repository at https://github.com/9xg/flow-phantom.

3 Results

3.1 *Flow System Characterization*

Eleven different tubes were assessed for their photoacoustic imaging suitability (Fig. 2). Tubes made from PMMA (I.D./O.D. 375/500, 432/865, 667/1000) showed the lowest signal-to-background (SBR) ratios ranging from 0.15 to 0.37. The other tubes materials show a clear trend of increasing SBR with larger inner diameters. Silicone tubes present high SBRs, even for low I.D./O.D. ratios (300/600, 630/1190, and 1570/2410). Three tubes showed very similar performance (I.D./O.D. 1500/2100, 1570/2410, and 2660/2800). The PVC tube with 1500/2100 presented a uniform, circular appearance in images with high SBR; it was therefore selected for the remaining experiments. Note also that regions of interest (ROIs) indicated in Fig. 2(a) exclude an outer boundary, but the dimensions of the image suggest that this boundary is likely to be due to the low

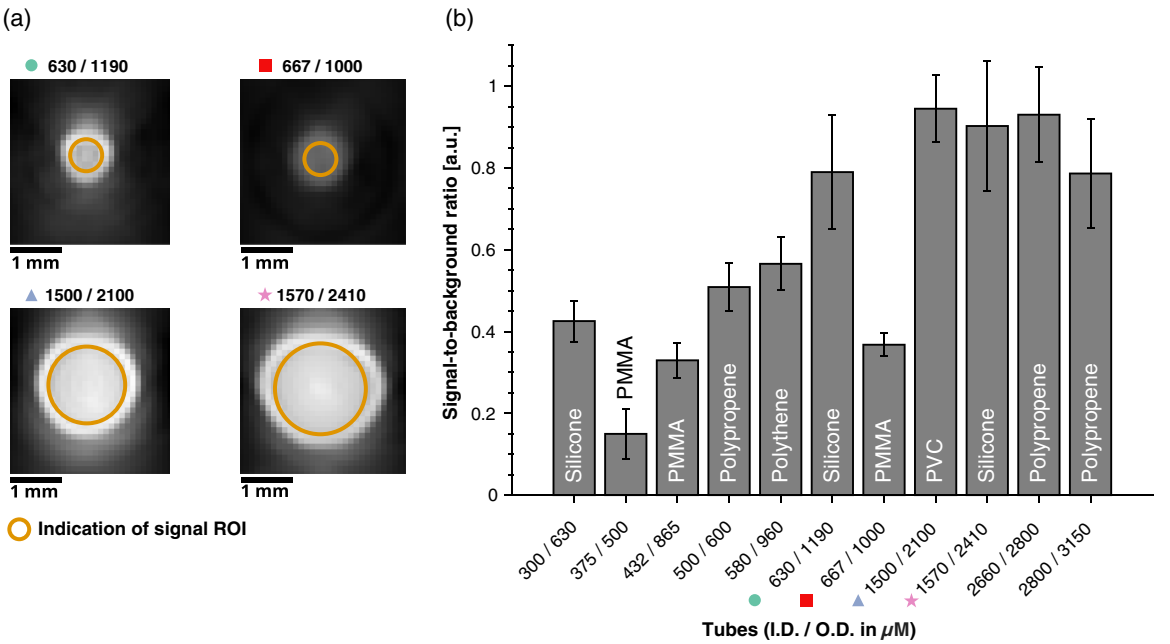

Fig. 2 Assessment of the effect of tube type on the quality of photoacoustic images. (a) PAT images (at 775 nm) of four tubes with inner and outer diameters (I.D.-O.D.) in μm of 630 to 1190 (silicone), 667 to 1000 (PMMA), 1500 to 2100 (PVC), and 1570 to 2410 (silicone), filled with a solution of ICG and embedded within a scattering agar cylinder (not shown). (b) Mean photoacoustic signal intensity inside the tube relative to the signal outside (SBR) for 11 different tubes. The tube with I.D.-O.D. 1500 to 2100 μm was selected due to its high SBR, flexibility, and low cost. The four tubes illustrated in (a) are marked with symbols.

frequency response of the detectors rather than absorption by the tube wall itself.

Dilutions of MB and ICG were tested inside the flow phantom under closed conditions, i.e., with a steady concentration flowing in the circuit. By calculating the mean PA signal intensities over a manually segmented tube cross-sectional ROI for 17 different wavelengths, it was possible to compare the PA spectra with those acquired during online flow spectrometry [Figs. 3(a)–3(d)]. Unexpectedly, the two independent spectral measurements show poor agreement in terms of relative intensities and spectral shape for the different dye concentrations. In particular, it is notable that the PA signal intensities [Fig. 3(b)] show a more pronounced shift in spectral peak with increasing ICG concentration compared with the online spectrometer data [Fig. 3(d)]; this may be a result of spectral coloring where light attenuation at the 800-nm peak suppresses the PA signal intensity deeper within the tube, leading to an overall reduction in mean PA intensity at this wavelength. Long fluorescent lifetimes and formation of aggregates are additional factors that may influence the inversion of the PA spectrum, although they do not explain the absence of an equivalent spectral shift in the spectrometer data. For MB, the discrepancies are difficult to discern seeing as the prominent spectral features occur below the PA imaging range. However, it is interesting that the relative PA intensities are about half those for ICG suggesting that MB has poorer PA signal generation efficiency; this may be related to the long-lived triplet states of MB, which tend to suppress PA emission and can in fact be exploited in pump-probe techniques to enhance the PA signal.[36,37] Overall, these spectral inconsistencies raise a question about which are the most suitable endmember spectra for unmixing PAT images of MB and ICG.

The spectra measured with the online spectrometer and offline in the plate reader were used to perform concentration-specific unmixing of the mean ROI intensities recorded at all 17 wavelengths, and these unmixed intensities were compared with those calculated using the literature spectra incorporated within the PA analysis software. These literature spectra are

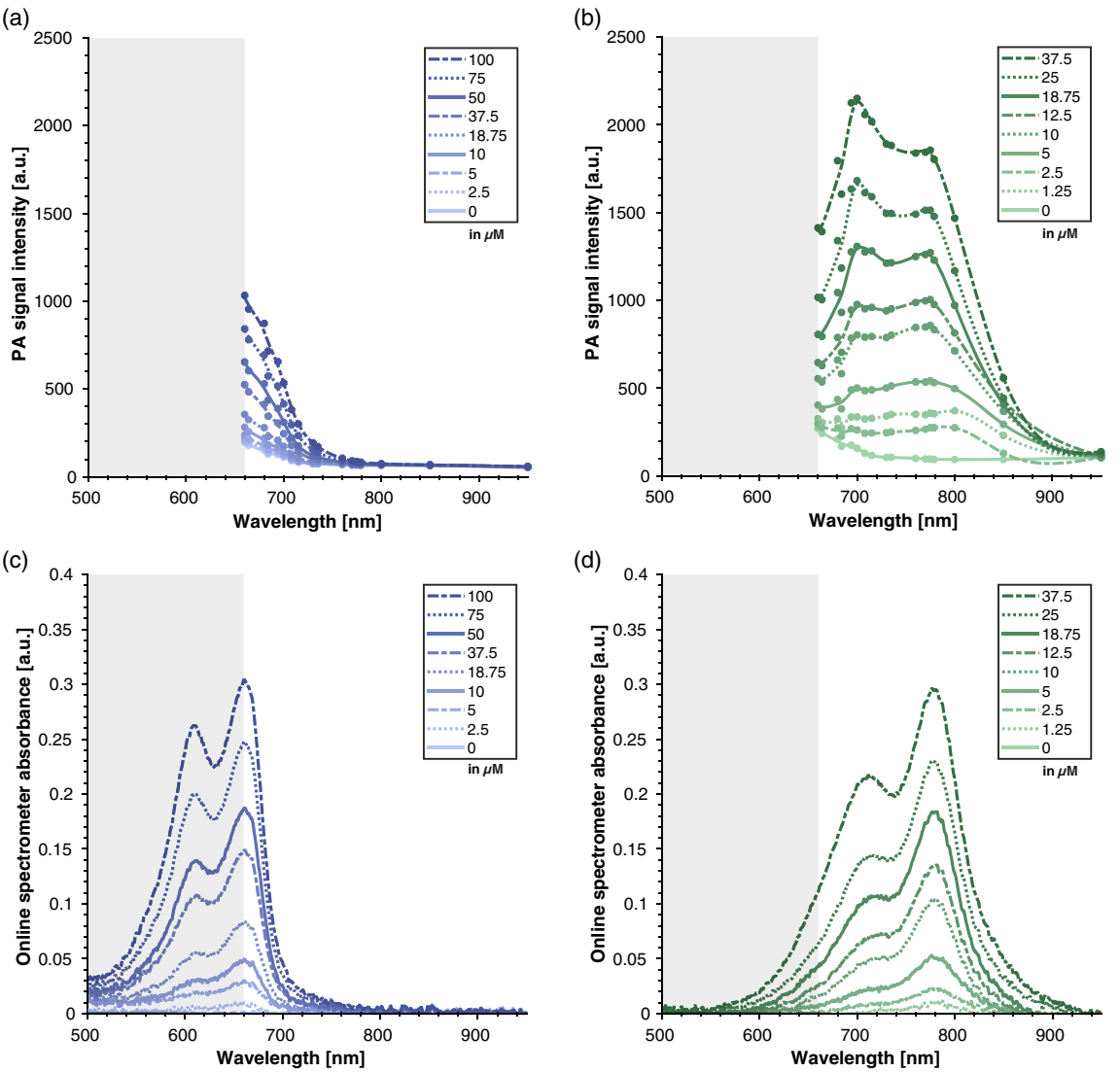

Fig. 3 Comparison of dye spectra measured using PAT and online flow spectrometry under closed conditions. (a), (b) PA signal intensities (with smoothed spline) and (c), (d) online flow spectrometer absorbance values measured for different concentrations of MB [panels (a) and (c)] and ICG [panels (b) and (d)]. Gray box indicates wavelengths outside the PAT spectral range.

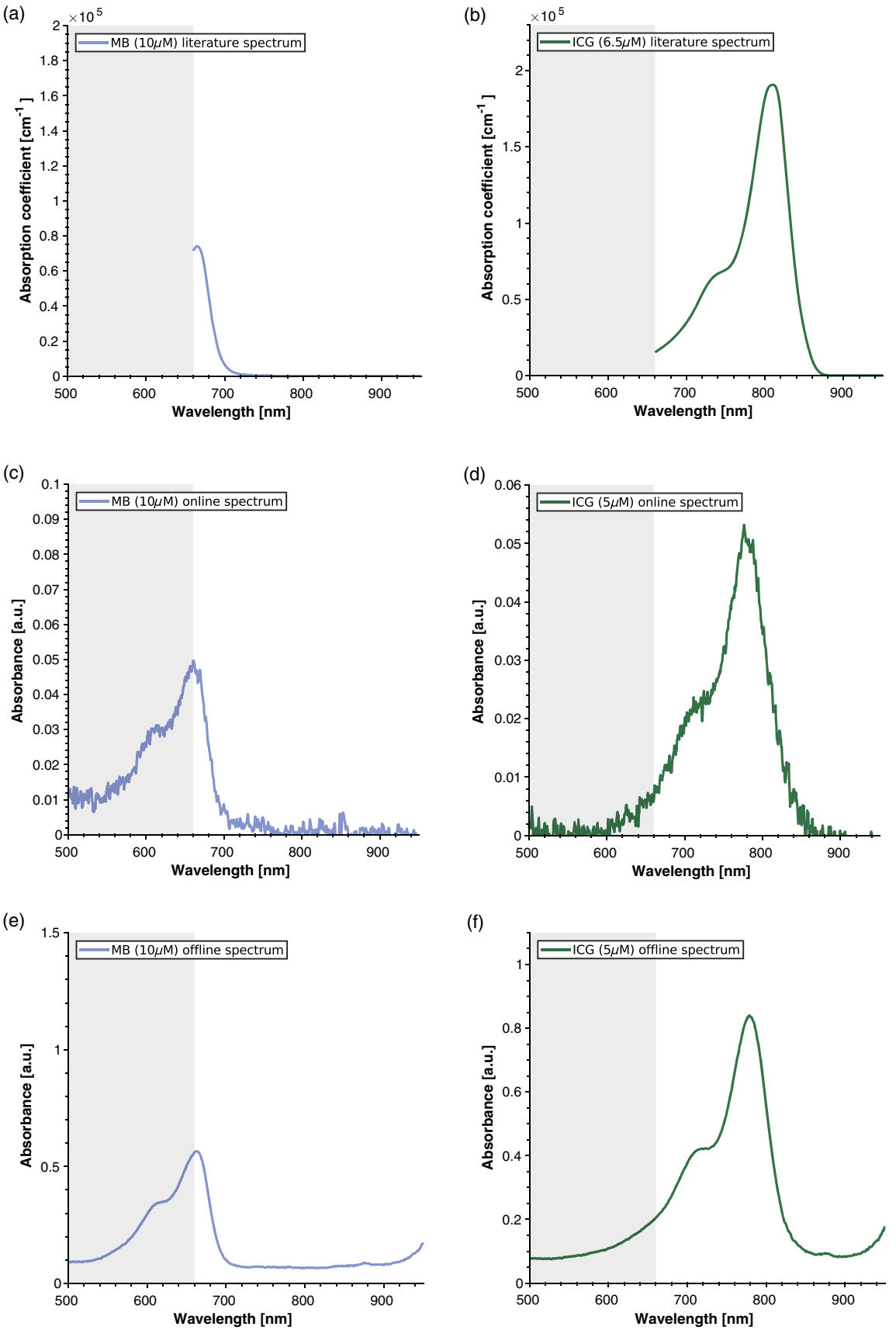

Fig. 4 Comparison of endmember spectra used for spectral unmixing. (a), (b) Literature spectra, spectra acquired using (c), (d) the online flow spectrometer and (e), (f) the offline flow spectrometer for MB [panels (a), (c), and (e)] and ICG [panels (b), (d), and (f)].

shown in Figs. 4(a)–4(b) along with online and offline spectra for example concentrations [Figs. 4(c)–4(f)].

Figures 5(a) and 5(b) show a linear relationship between dye concentration and spectrally unmixed PA intensities up to 100 μmol for MB and 40 μmol for ICG, respectively. Divergence between the two types of unmixing is likely due to concentration-dependent changes in the spectra of these dyes; these changes are particularly prominent for ICG and indeed the online spectra [Fig. 3(d)] slightly deviate from a linear relationship with increasing concentration.

Having explored the application of the flow circuit under static concentration values, we then examined the response of the PAT instrument to dynamic changes in dye concentrations for MB and ICG [Figs. 5(c) and 5(d)]. PA images were unmixed using the literature spectra and those recorded live using the online spectrometer, and then converted to absolute concentration values using the linear models (LM) calculated and plotted in Figs. 5(a) and 5(b). Neglecting the initial lag phase (which could not be experimentally determined and therefore was not incorporated into the model), the rates of concentration change match reasonably well with those predicted by the model [Eq. (5)]. However, there is a notable discrepancy between the dynamics calculated using the literature and online spectra for ICG unmixing; if the lag phase were corrected for, the online unmixing would be the closer match to the model and this is again likely to be a consequence of the concentration-dependent change in spectral shape, which is incorporated in the online spectra but not the single literature spectrum.

3.2 *Blood Oxygenation Measurements*

To demonstrate the closed nature of the blood flow circuit, blood was fully oxygenated by adding approximately 15 μL 0.2% v/v H_2O_2 to 8-mL mouse blood and then injecting this into the flow

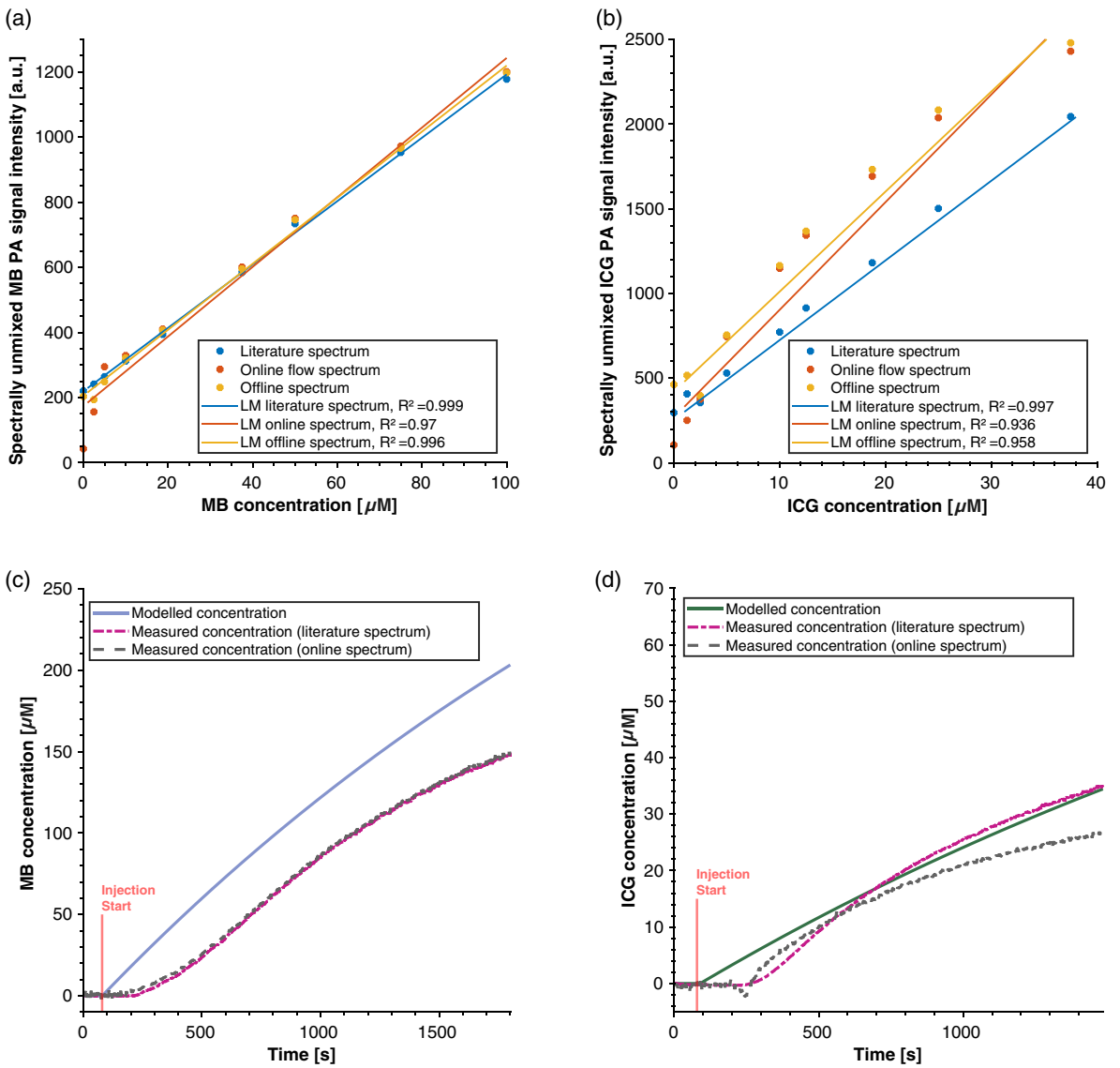

Fig. 5 Spectrally unmixed PA signal intensities for a range of dye concentrations. (a) MB and (b) ICG concentrations obtained by unmixing with literature spectra and those measured using the online and offline spectrometers. The LM was used to calculate concentrations of (c) MB and (d) ICG during evolution of dye concentrations within the flow circuit due to continual dye injection. The starting points were forced to zero for ease of comparison.

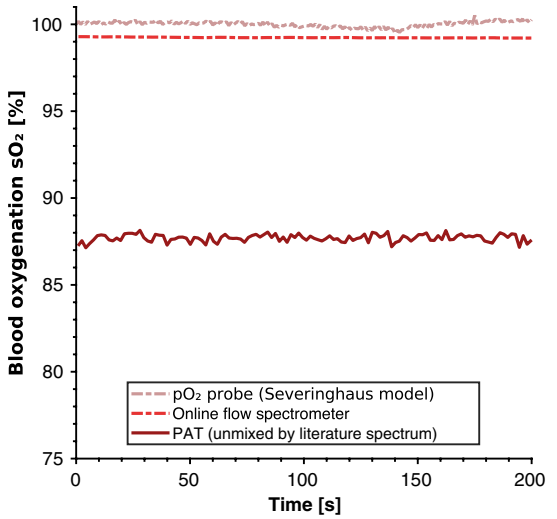

Fig. 6 Assessment of blood oxygenation within the flow circuit under closed conditions. Blood oxygen saturation (sO_2) was calculated using the three independent methods: the pO_2 probe measurements [using Eq. (2)]; unmixing of the spectra measured using the online flow spectrometer (with experimentally measured spectra as end-members); unmixing of the mean pixel intensities in the PA images (with literature spectra as end-members) acquired while blood circulated in the flow system for 200 s.

system and circulating it for several minutes. Figure 6 shows the blood oxygen saturation (sO_2) measured within the flow circuit by: the pO_2 probe, the online spectrometer, and PAT. The sO_2 was calculated from the pO_2 data using Eq. (2) and from the online spectrometer and PAT data through spectral unmixing. To enable comparison between the methods independently, unmixing was performed using the spectra inherent to each system: for the online spectrometer, experimentally measured spectra were used as endmembers, whereas for PAT data, the literature spectra were used. As hoped, all three sO_2 measurements show consistent values over time. However, the sO_2 calculated from the unmixed PA images under-reads by about 13% compared to the ground truth sO_2 calculated from the pO_2 probe and the online flow spectrometer.

In addition to investigating static blood oxygenation within the circuit, the full range of blood sO_2 values (100% to 0%) were explored by injecting sodium hydrosulfite into the flow circuit in order to gradually deoxygenate the blood. The blood sO_2 values cover the expected dynamic range when calculated from both the pO_2 probe and the online spectrometer [Fig. 7(a)]; however, PA signal intensities show markedly different behaviors when unmixed with spectra [Fig. 7(b)] from the literature or from the online flow spectrometer. The sO_2 values calculated by unmixing with the experimentally measured spectra [gray dotted line, Fig. 7(a)] show good agreement with the spectrometer-derived ground truth values [orange/red line, Fig. 7(a)], except for somewhat over-reading the oxygenation for sO_2 values below about 20%. They also show a dynamic range comparable to that obtained from the pO_2 probe and Severinghaus model. However, the sO_2 values calculated by unmixing with the literature spectra [pink dashed line, Fig. 7(a)] surprisingly exhibit a dramatically reduced dynamic range (86% to 58%); this may be due to the unmixing spectra and/or spectral coloring.

Two further investigations explored the potential impact of spectral colouring. First, spatially resolved sO_2 measurements were calculated [Fig. 8(a)]. Unlike the results in Figs. 6 and 7 that were calculated from the mean of the ROI defined on the tube cross-sectional area, the results in Fig. 8(a) entailed unmixing first using the wavelength-dependent intensities of the single pixel at the tube center, and then repeatedly unmixing for the mean intensities of pixels found in circles increasing in one pixel (75 μm) increments toward the perimeter of the ROI. For the fully oxygenated blood, the sO_2 values are consistent across the tube diameter, but as the blood becomes deoxygenated there is a clear trend toward sO_2 over-reading at the center of the tube; this is a clear demonstration of spectral coloring. A second

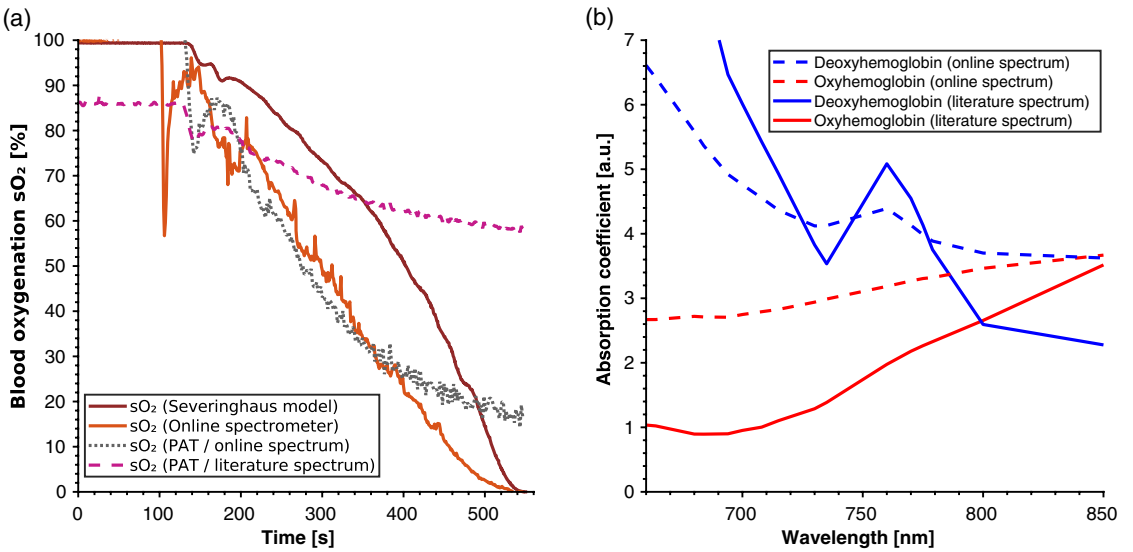

Fig. 7 Dynamic deoxygenation of the circulating blood. (a) Change in blood oxygen saturation (sO_2) measured using the pO_2 probe, online spectrometer, and PAT system while injecting 3% w/v sodium hydrosulfite in PBS over a period of 9 min. The anomalous data for the online spectrometer around 100 s may be due to a small bubble passing through the circuit. (b) Literature spectra for oxy- and deoxy-hemoglobin used for spectral unmixing,[7] compared to spectra obtained from the online spectrometer at the start and end of dynamic deoxygenation.

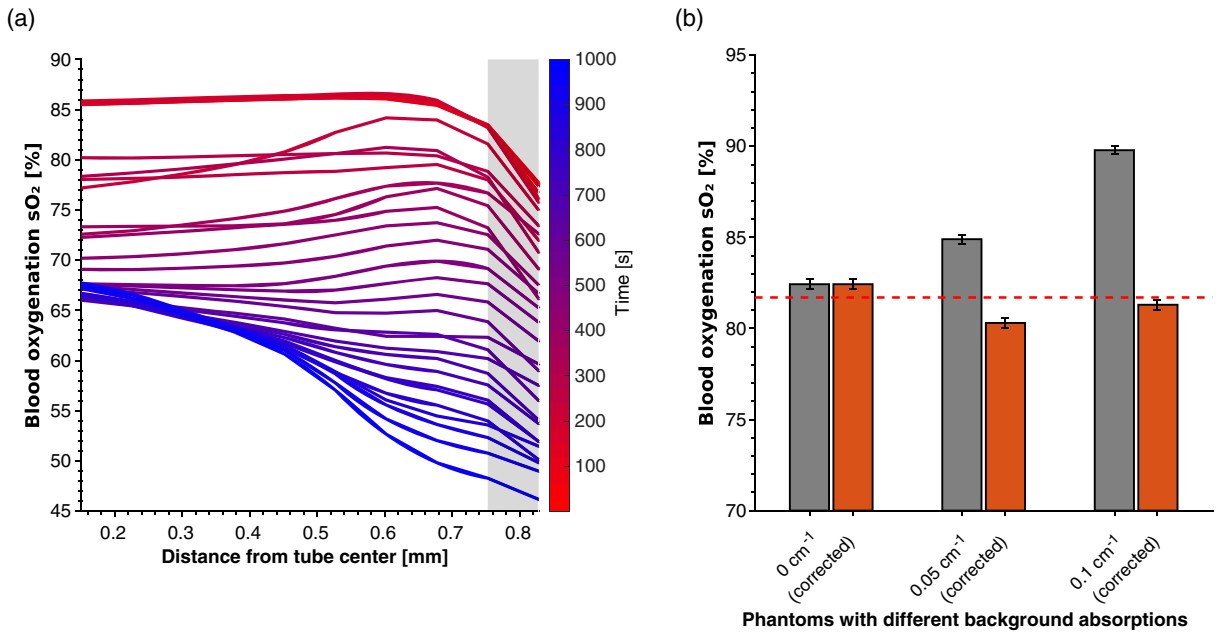

Fig. 8 Investigation of spectral coloring. (a) Spatial profiles of blood oxygen saturation (sO_2) as a function of distance from the center of the flow circuit tube by PA unmixing with spectra measured using the online spectrometer during dynamic blood oxygenation (Fig. 7). (b) Impact of correction for the absorption spectrum of the nigrosin dye included in the background of the tissue-mimicking phantom as a function of dye concentration. For absorption coefficients of >0 cm^{-1}, the sO_2 (gray bars) deviated from the ground truth value (dotted line); accurate values were restored by recalculating sO_2 (orange bars) after dividing the photoacoustic images by the relevant nigrosin spectrum as described in the text.

illustration of spectral coloring is shown in Fig. 8(b) where experiments were repeated with absorbing nigrosin dye incoporated into the background of the tissue-mimicking phantom surrounding the flow circuit tube; in all the previous experiments, the agar background was optically scattering but assumed to have negligible absorption. Increasing the background absorption causes increasing inaccuracy of the sO_2 relative to the ground truth since wavelengths of light are preferentially absorbed by the nigrosin dye, leading to overestimation of the contribution of oxyhemoglobin to the PA signal. A simple light fluence correction, implemented by dividing the images by the known nigrosin spectrum (Sec. 2.4), restored consistent sO_2 measurements irrespective of the background absorption, providing evidence that this over-reading phenomenon is indeed related to spectral coloring.

4 Discussion

The application of PAT in assessment of blood hemoglobin concentration and oxygen saturation is now widespread, but estimation of the oxy- and deoxyhemoglobin chromophore concentrations is affected by a variety of tissue- and instrumentation-dependent factors. We have developed and applied a low-cost flow phantom system with online monitoring of optical absorption spectra and partial pressure of oxygen in order to facilitate testing of PAT systems.

We first selected an appropriate tubing to maximize PAT image quality and tested the circuit using two optically absorbing dyes. For both dyes, MB and ICG, the absorption spectrum exhibits a double peak where the relative peak intensities shift with increasing concentration. Unmixing with a single "average" spectrum is therefore unlikely to yield the same result as unmixing with a concentration-specific (online/offline) spectrum; indeed, we observed different and slightly nonlinear relationships between dye concentration and spectrally unmixed intensities (which are assumed to be proportional to concentration) for the two types of unmixing. For ICG, the values from unmixing with the literature spectrum under-read those from unmixing with the online/offline spectra [Figs. 5(b) and 5(d)]; for MB the unmixing results were indistinguishable [Figs. 5(a) and 5(c)] since the concentration-dependent effects occur outside of the wavelength range of the PA system under test. It is possible that erroneous concentration measurements may also be caused by spectral coloring, even though only a single component is used in the spectral unmixing; two component unmixing (Hb and HbO_2) is more relevant for calculation of sO_2.

We proceeded to evaluate the estimation of sO_2 under both closed circuit and dynamic conditions. The results highlight two major factors that contribute to inaccuracies in spectral unmixing, and therefore in sO_2 measurements. The first is the choice of spectra for unmixing the photoacoustic images; the second is the effect of spectral coloring. The online spectrometer allowed spectra to be recorded during PAT image acquisition and used as alternatives to published spectra for unmixing the images. Moreover, the ground truth sO_2 values provided by the spectrometer and the pO_2 probes are designed to facilitate exploration of phenomena such as spectral coloring.

Images of blood flowing through the circuit entailed unmixing with two components: oxy- and deoxyhemoglobin. The resulting sO_2 calculations (HbO_2/THb) were consistent over time but were dependent on the hemoglobin spectra used for unmixing, the blood oxygenation saturation, and also the position within the tube. The spectra for oxy- and deoxyhemoglobin measured online were considerably different from those available in the literature that are widely used for spectral unmixing,

both *in vitro* and *in vivo*. This could be attributed to optical scattering due to the blood cells within the measurement cuvette, as literature studies normally measure the hemoglobin molecule directly. The online flow spectrometer spectra can therefore be described as attenuation spectra, incorporating both absorption and scattering, and using these instead of the literature absorption spectra improved the accuracy of the sO_2 calculations.

Over-reading of the lowest sO_2 values was also observed and attributed to spectral coloring: the high absorption by deoxygenated blood at wavelengths below about 750 nm results in low light intensities at these wavelengths in the center of the tube and therefore the PA intensities (proportional to both absorption and light fluence) varied with wavelength in a way more closely matching with oxyhemoglobin, leading to overestimation of the oxyhemoglobin concentration. Although this spectral distortion occuring within the tube was not corrected, a simple example of correcting the effects of spectal coloring introduced by the tissue-mimicking phantom surrounding the tube was achieved through dividing by the background nigrosin spectrum, which restored accurate sO_2 measurements.

One limitation of the study is the discrepancy between our measured hemoglobin spectra and those widely used in the literature. Lysing the blood cells would obviate optical scattering and the resulting absorption (rather than attenuation) spectra would therefore be more comparable with those in the literature. Future experiments should also calibrate the measured spectra by extracting blood samples from the circuit at different sO_2 values and validating the sO_2 using a blood gas analyzer. A further limitation arises from the pO_2 measurements, as the dynamics of the deoxygenation study did not directly mirror the sO_2 values obtained in the spectrometer. This may be due to an unrepresentative conversion from pO_2 to sO_2: the Severinghaus equation is derived from human, not mouse, blood data, and also assumes certain values for parameters such as pH and temperature. Alternative conversions such as the Kelman equation were also explored, and measured values for pH and temperature were incorporated, but this did not significantly alter the trend in sO_2 over time. It is possible that bubbles or insufficient contact with the blood in the circuit corrupted the pO_2 readings, and therefore future versions of the circuit will integrate truly in-flow pO_2 probes and a membrane oxygenator to avoid bubbles.

The application of the presented phantom opens a range of opportunities for future studies of tissue- and instrument-dependent correction factors in PAT. In particular, future work will attempt to model and account for the spectral distortion across the tube diameter observed during blood oxygenation studies. To eliminate the possibility that the tube wall itself contributes to the photoacoustic signal, future studies will also explore the use of a wall-less phantom. The development of corrections incorporating multiple choromphores inside and outside the tube both *ex vivo* and *in vivo* is more complex and continues to be investigated, for example, using Monte Carlo simulations and model-based iterative minimisation.[14,15,17,19–21] Moreover, the number and choice of wavelengths used for spectral unmixing is an important consideration[38] to be investigated in future work.

5 Conclusion

In summary, we have developed a low-cost flow phantom that includes an online spectrometer and partial pressure of oxygen probe to facilitate detailed validation of PAT measurements of blood oxygen saturation, sO_2. We found that it is important to correctly identify the absorption (or attenuation) spectra to be used for unmixing photoacoustic images in order to accurately determine even relative absorber concentrations. We also found that the codependence of photoacoustic signal intensity on light fluence and absorption leads to a major challenge in accounting for spectral coloring, which can lead to substantial underestimation of sO_2. Further calibration and automation of the circuit will enable additional *ex vivo* studies requiring careful control and knowledge of blood sO_2, as well as opening the possibility of exploring additional blood parameters such as pH, and also absorptive and other properties of different fluids. Detailed understanding of the photoacoustic signal origins *ex vivo* remains essential for proper interpretation of photoacoustic measurements made *in vivo*.

Disclosures

SEB has received research support from iThera Medical GmbH and PreXion Inc., vendors of photoacoustic imaging instruments.

Acknowledgments

The authors would like to thank Ayaka Shinozaki for her assistance with data collection, James Joseph for his contributions to the experimental design, and Michael Schneider for his helpful input regarding data interpretation. This work was supported by Cancer Research UK (C47594/A16267, C14303/A17197) and the EPSRC-CRUK Cancer Imaging Centre in Cambridge and Manchester (C197/A16465 and C8742/A18097). We would like to thank the CRUK CI Core Facilities for their support of this work, in particular the Imaging Core and the Biological Resource Unit.

References

1. M. Martinho Costa et al., "Quantitative photoacoustic imaging study of tumours in vivo: baseline variations in quantitative measurements," *Photoacoustics* **13**, 53–65 (2019).
2. I. Quiros-Gonzalez et al., "Optoacoustics delineates murine breast cancer models displaying angiogenesis and vascular mimicry," *Br. J. Cancer* **118**, 1098–1106 (2018).
3. J. Yang et al., "Photoacoustic imaging for the evaluation of early tumor response to antivascular treatment," *Quant. Imaging. Med. Surg.* **9**(2), 160–170 (2019).
4. M. J. Waldner et al., "Multispectral optoacoustic tomography in Crohn's disease: noninvasive imaging of disease activity," *Gastroenterology* **151**(2), 238–240 (2016).
5. N. Bhutiani et al., "Noninvasive imaging of colitis using multispectral optoacoustic tomography," *J. Nucl. Med.* **58**(6), 1009–1012 (2017).
6. H. F. Zhang et al., "Imaging of hemoglobin oxygen saturation variations in single vessels *in vivo* using photoacoustic microscopy," *Appl. Phys. Lett.* **90**(5), 053901 (2007).
7. S. Prahl, "Optical absorption of hemoglobin," 1999, https://omlc.org/spectra/hemoglobin/.
8. S. Prahl, "Methylene blue spectra," 2017, https://omlc.org/spectra/mb/.
9. M. Landsman et al., "Light-absorbing properties, stability, and spectral stabilization of indocyanine green," *J. Appl. Physiol.* **40**(4), 575–583 (1976).
10. K. Maslov, H. F. Zhang, and L. V. Wang, "Effects of wavelength-dependent fluence attenuation on the noninvasive photoacoustic imaging of hemoglobin oxygen saturation in subcutaneous vasculature *in vivo*," *Inverse Prob.* **23**, S113–S122 (2007).
11. B. Cox et al., "Quantitative spectroscopic photoacoustic imaging: a review," *J. Biomed. Opt.* **17**(6), 061202 (2012).
12. T. Mitcham et al., "Photoacoustic-based SO_2 estimation through excised bovine prostate tissue with interstitial light delivery," *Photoacoustics* **7**, 47–56 (2017).

13. J. Laufer et al., "*In vitro* measurements of absolute blood oxygen saturation using pulsed near-infrared photoacoustic spectroscopy: accuracy and resolution," *Phys. Med. Biol.* **50**, 4409–4428 (2005).
14. B. Cox et al., "Two-dimensional quantitative photoacoustic image reconstruction of absorption distributions in scattering media by use of a simple iterative method," *Appl. Opt.* **45**(8), 1866–1875 (2006).
15. Z. Yuan and H. Jiang, "Quantitative photoacoustic tomography: recovery of optical absorption coefficient maps of heterogeneous media," *Appl. Phys. Lett.* **88**(23), 231101 (2006).
16. J. Laufer et al., "Quantitative spatially resolved measurement of tissue chromophore concentrations using photoacoustic spectroscopy: application to the measurement of blood oxygenation and haemoglobin concentration," *Phys. Med. Biol.* **52**, 141–168 (2007).
17. J. Laufer et al., "Quantitative determination of chromophore concentrations from 2D photoacoustic images using a nonlinear model-based inversion scheme," *Appl. Opt.* **49**, 1219–1233 (2010).
18. Y. Liu, H. Jiang, and Z. Yuan, "Two schemes for quantitative photoacoustic tomography based on Monte Carlo simulation," *Med. Phys.* **43**(7), 3987–3997 (2016).
19. L. Yao, Y. Sun, and H. Jiang, "Quantitative photoacoustic tomography based on the radiative transfer equation," *Opt. Lett.* **34**, 1765–1767 (2009).
20. F. M. Brochu et al., "Towards quantitative evaluation of tissue absorption coefficients using light fluence correction in optoacoustic tomography," *IEEE Trans. Med. Imaging* **36**, 322–331 (2017).
21. B. T. Cox, S. R. Arridge, and P. C. Beard, "Estimating chromophore distributions from multiwavelength photoacoustic images," *J. Opt. Soc. Am. A* **26**(2), 443–455 (2009).
22. S. Tzoumas et al., "Eigenspectra optoacoustic tomography achieves quantitative blood oxygenation imaging deep in tissues," *Nat. Commun.* **7**(May), 12121 (2016).
23. W. C. Vogt et al., "Biologically relevant photoacoustic imaging phantoms with tunable optical and acoustic properties," *J. Biomed. Opt.* **21**(10), 101405 (2016).
24. E. Maneas et al., "Gel wax-based tissue-mimicking phantoms for multispectral photoacoustic imaging," *Biomed. Opt. Express* **9**(3), 1151–1163 (2018).
25. R. O. Esenaliev et al., "Optoacoustic technique for noninvasive monitoring of blood oxygenation: a feasibility study," *Appl. Opt.* **41**(22), 4722–4731 (2002).
26. W. C. Vogt et al., "Photoacoustic oximetry imaging performance evaluation using dynamic blood flow phantoms with tunable oxygen saturation," *Biomed. Opt. Express* **10**(2), 449–464 (2019).
27. S. N. Hennen et al., "Photoacoustic tomography imaging and estimation of oxygen saturation of hemoglobin in ocular tissue of rabbits," *Exp. Eye Res.* **138**, 153–158 (2015).
28. Z. Chen, S. Yang, and D. Xing, "*In vivo* detection of hemoglobin oxygen saturation and carboxyhemoglobin saturation with multiwavelength photoacoustic microscopy," *Opt. Lett.* **37**(16), 3414–3416 (2012).
29. Y. Wang et al., "*In vivo* integrated photoacoustic and confocal microscopy of hemoglobin oxygen saturation and oxygen partial pressure," *Opt. Lett.* **36**(7), 1029–1031 (2011).
30. J. W. Severinghaus, "Simple, accurate equations for human blood O_2 dissociation computations," *J. Appl. Physiol. Respir. Environ. Exerc. Physiol.* **46**(3), 599–602 (1979).
31. J.-A. Collins et al., "Relating oxygen partial pressure, saturation and content: the haemoglobin-oxygen dissociation curve," *Breathe* **11**, 194–201 (2015).
32. D. White and P. Teasdale, "The oxygenation of blood by hydrogen peroxide," *Br. J. Anaesth.* **36**, 528–529 (1964).
33. K. Briely-Sabo and A. Bjornerud, "Accurate de-oxygenation of ex vivo whole blood using sodium dithionite," *Proc. Int. Soc. Magn. Reson. Med.* **117**(1985), 2025 (2000).
34. S. Tzoumas et al., "Unmixing molecular agents from absorbing tissue in multispectral optoacoustic tomography," *IEEE Trans. Med. Imaging* **33**(1), 48–60 (2014).
35. L. Ding et al., "Constrained inversion and spectral unmixing in multispectral optoacoustic tomography," *IEEE Trans. Med. Imaging* **36**, 1676–1685 (2017).
36. S. Ashkenazi, "Photoacoustic lifetime imaging of dissolved oxygen using methylene blue," *J. Biomed. Opt.* **15**(4), 040501 (2010).
37. E. Morgounova et al., "Photoacoustic lifetime contrast between methylene blue monomers and self-quenched dimers as a model for dual-labeled activatable probes," *J. Biomed. Opt.* **18**(5), 056004 (2013).
38. R. Hochuli, P. C. Beard, and B. Cox, "Effect of wavelength selection on the accuracy of blood oxygen saturation estimates obtained from photoacoustic images," *Proc. SPIE* **9323**, 93231V (2015).

Marcel Gehrung received his MSc degree from Eberhard Karls University Tuebingen in 2017 and is currently pursuing his PhD in medical science at the University of Cambridge focused on the application of machine learning methods for cancer diagnosis.

Sarah E. Bohndiek received her BA degree from the University of Cambridge in 2005 and her PhD in radiation physics from the University College London in 2008, specializing in x-ray diffraction. After postdoctoral fellowships in both the UK and USA, she started the VISIONLab in Cambridge in 2013, which develops and applies new imaging biomarkers to shed light on the tumour microenvironment.

Joanna Brunker received her MSc degree in natural sciences in 2009 and her PhD in medical physics and biomedical engineering from the University College London, United Kingdom, in 2013. Following her postdoctoral research fellowships at UCL and at the Cancer Research UK Cambridge Institute, in July of 2019 she started a research group at the UCL Wellcome/EPSRC Centre for Interventional and Surgical Sciences (WEISS) where she will focus on translation of photoacoustic and other imaging technologies into clinical practice.